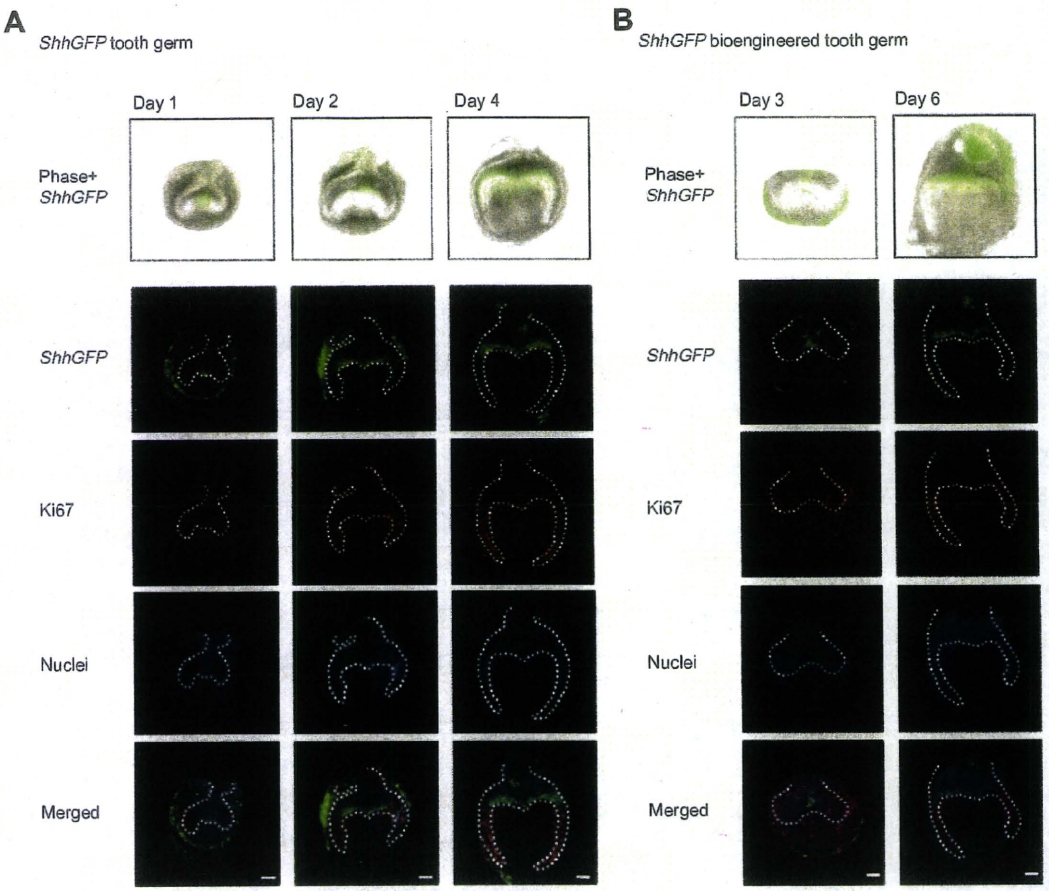

Fig. 4. The spatiotemporal epithelial cell growth correlates with the *Shh* expression area and is involved the regulation of crown size. (A) Molar germs isolated from an *ShhGFP* mouse at ED14.5 after 1, 2, and 4 days of organ culture. (B) *ShhGFP* bioengineered tooth germs, which were generated from the molar germs of an *ShhGFP* mouse at ED14.5, were examined after 3 and 6 days of organ culture. *Shh* expression was visualized by the detection of GFP signals. Cell proliferation was immunohistochemically analyzed using a specific antibody against Ki67. Nuclei were detected by staining with Hoechst33342. Dotted lines indicate the boundaries between the epithelium and mesenchyme. Scale bars, 100 μm.

formation, and might be regulated by the interaction between FGF4, as an activator of cusp formation, and the BMPs and SHH as inhibitors [19]. Based on an earlier computational model of mammalian tooth development, there may be a simple basis for the variations in cusp patterning which can be explained by changes in single model parameters [12,20]. Although there are several reports regarding the determination of tooth size and cusp number, the mechanisms suggested in these studies remain controversial. It was previously reported that each tooth and cusp size is determined by each mesenchyme and epithelium, respectively, through species-specific biological programs [10]. It has also been suggested that the number of developing cusps of a tooth reconstituted from dental epithelium and dissociated mesenchymal cells was enlarged by increasing the mesenchymal cell number [21]. Furthermore, it has been suggested that the number of cusps, a micro-patterning event, is regulated by waves which are determined by the tooth size i.e. macro-patterning, in a reaction-diffusion model [10]. Our present findings indicate that the cusp number in a bioengineered tooth is significantly correlated with the crown width, which is regulated by the contact area between the epithelial and mesenchymal cell layers. These findings suggest that the micro-patterning of cusp formation is regulated after tooth size determination (i.e. macro-patterning) through the number and length of waves in a reaction-diffusion model.

Currently, it is anticipated that organ replacement therapy will represent the next generation of regenerative medical technology and successfully replace lost or damaged organs [22]. For such replacement tissues to function correctly, it will be necessary to reproduce the organ mass through the generation of a sufficient number of functional cells, and faithful replication of both the macro- and micro-morphologies [23]. As a concept for organ regeneration, an approach to developing a functional bioengineered organ from a bioengineered organ germ by reproducing the developmental process during organogenesis has now been investigated [4,24]. We have also previously reported from our laboratory that a bioengineered tooth germ reconstituted using an organ germ method can regenerate a fully functional bioengineered tooth through transplantation [14]. It is thought that the regulation of a bioengineered tooth morphology, such as the crown size and the number and location of the cusps, is important for occlusion to properly occur [11], which is an essential issue for future tooth regenerative therapy [4,24]. Previously, it has been reported that the morphology of a bioengineered tooth can be regulated by culturing tooth germ cells onto a tooth-shaped biodegradable scaffold [24]. In our present study, our cell manipulation technique to regulate the contact area between epithelial and mesenchymal cell layers will make a substantial contribution to the future clinical application of bioengineered teeth.

Our present data suggest that the spatiotemporal patterning of cell proliferation and *Shh* expression areas in the epithelium regulates the crown width and cusp formation of the tooth. Further studies of the molecular mechanisms underlying cell proliferation, differentiation and cell movement will contribute further to our understanding of tooth organogenesis. The development of future

technologies to more precisely regulate the morphology of bioengineered teeth will be required to realize tooth regenerative therapy.

Acknowledgments

This work was partially supported by Health and Labour Sciences Research Grants from the Ministry of Health, Labour, and Welfare (No. 21040101), a Grant-in-Aid for Scientific Research in Priority Areas (No. 50339131), a Grant-in-Aid for Scientific Research (A) from Ministry of Education, Culture, Sports and Technology, Japan (all to T.T.).

References

[1] J. Pispa, I. Thesleff, Mechanisms of ectodermal organogenesis, Dev. Biol. 262 (2003) 195–205.
[2] I. Thesleff, Epithelial–mesenchymal signalling regulating tooth morphogenesis, J. Cell Sci. 116 (2003) 1647–1648.
[3] A. Tucker, P. Sharpe, The cutting-edge of mammalian development; how the embryo makes teeth, Nat. Rev. Genet. 5 (2004) 499–508.
[4] P.T. Sharpe, C.S. Young, Test-tube teeth, Sci. Am. 293 (2005) 34–41.
[5] S.F. Gilbert, Developmental Biology, ninth ed., Sinauer, Massachusetts, 2010.
[6] A. Gritli-Linde, M. Bei, R. Maas, X.M. Zhang, A. Linde, A.P. McMahon, Shh signaling within the dental epithelium is necessary for cell proliferation, growth and polarization, Development 129 (2002) 5323–5337.
[7] M.I. Cho, P.R. Garant, Development and general structure of the periodontium, Periodontology 2000 (24) (2000) 9–27.
[8] K.D. Kavanagh, A.R. Evans, J. Jernvall, Predicting evolutionary patterns of mammalian teeth from development, Nature 449 (2007) 427–432.
[9] Z. Zhang, Y. Lan, Y. Chai, R. Jiang, Antagonistic actions of Msx1 and Osr2 pattern mammalian teeth into a single row, Science 323 (2009) 1232–1234.
[10] J. Cai, S.W. Cho, J.Y. Kim, M.J. Lee, Y.G. Cha, H.S. Jung, Patterning the size and number of tooth and its cusps, Dev. Biol. 304 (2007) 499–507.
[11] J. Jernvall, I. Thesleff, Reiterative signaling and patterning during mammalian tooth morphogenesis, Mech. Dev. 92 (2000) 19–29.
[12] I. Salazar-Ciudad, J. Jernvall, A gene network model accounting for development and evolution of mammalian teeth, Proc. Natl. Acad. Sci. USA 99 (2002) 8116–8120.
[13] K. Nakao, R. Morita, Y. Saji, K. Ishida, Y. Tomita, M. Ogawa, M. Saitoh, Y. Tomooka, T. Tsuji, The development of a bioengineered organ germ method, Nat. Methods 4 (2007) 227–230.
[14] E. Ikeda, R. Morita, K. Nakao, K. Ishida, T. Nakamura, T. Takano-Yamamoto, M. Ogawa, M. Mizuno, S. Kasugai, T. Tsuji, Fully functional bioengineered tooth replacement as an organ replacement therapy, Proc. Natl. Acad. Sci. USA 106 (2009) 13475–13480.
[15] H.R. Dassule, P. Lewis, M. Bei, R. Maas, A.P. McMahon, Sonic hedgehog regulates growth and morphogenesis of the tooth, Development 127 (2000) 4775–4785.
[16] S. Kondo, A mechanistic model for morphogenesis and regeneration of limbs and imaginal discs, Mech. Dev. 39 (1992) 161–170.
[17] H.S. Jung, P.H. Francis-West, R.B. Widelitz, T.X. Jiang, S. Ting-Berreth, C. Tickle, L. Wolpert, C.M. Chuong, Local inhibitory action of BMPs and their relationships with activators in feather formation: implications for periodic patterning, Dev. Biol. 196 (1998) 11–23.
[18] Y. Litingtung, R.D. Dahn, Y. Li, J.F. Fallon, C. Chiang, Shh and Gli3 are dispensable for limb skeleton formation but regulate digit number and identity, Nature 418 (2002) 979–983.
[19] J. Jernvall, Linking development with generation of novelty in mammalian teeth, Proc. Natl. Acad. Sci. USA 97 (2000) 2641–2645.
[20] I. Salazar-Ciudad, J. Jernvall, A computational model of teeth and the developmental origins of morphological variation, Nature 464 (2010) 583–586.
[21] B. Hu, A. Nadiri, S. Kuchler-Bopp, F. Perrin-Schmitt, H. Peters, H. Lesot, Tissue engineering of tooth crown, root, and periodontium, Tissue Eng. 12 (2006) 2069–2075.
[22] R.I. Lechler, M. Sykes, A.W. Thomson, L.A. Turka, Organ transplantation - How much of the promise has been realized?, Nat Med. 11 (2005) 605–613.
[23] M.C. Raff, Size control: the regulation of cell numbers in animal development, Cell 86 (1996) 173–175.
[24] E. Ikeda, T. Tsuji, Growing bioengineered teeth from single cells: potential for dental regenerative medicine, Expert. Opin. Biol. Ther. 8 (2008) 735–744.

DENTAL MATERIALS 26 (2010) 524–532

available at www.sciencedirect.com

ScienceDirect

journal homepage: www.intl.elsevierhealth.com/journals/dema

TEM characterization of a silorane composite bonded to enamel/dentin

Atsushi Mine[a], *Jan De Munck*[a], *Annelies Van Ende*[a], *Marcio Vivan Cardoso*[a], *Takuo Kuboki*[b], *Yasuhiro Yoshida*[c], *Bart Van Meerbeek*[a,*]

[a] *Leuven BIOMAT Research Cluster, Department of Conservative Dentistry, School of Dentistry, Oral Pathology and Maxillo-Facial Surgery, Catholic University of Leuven, Kapucijnenvoer 7, B-3000 Leuven, Belgium*
[b] *Department of Oral and Maxillofacial Rehabilitation, Okayama University Graduate School of Medicine, Dentistry and Pharmaceutical Science, Okayama, Japan*
[c] *Department of Biomaterials, Okayama University Graduate School of Medicine, Dentistry and Pharmaceutical Science, Okayama, Japan*

ARTICLE INFO

Article history:
Received 25 June 2009
Accepted 26 January 2010

Keywords:
Adhesion
Low-shrinking composite
Silorane
Self-etch adhesive
Nano-interaction

ABSTRACT

Objectives. The low-shrinking composite composed of combined siloxane–oxirane technology (Filtek Silorane, 3M ESPE, Seefeld, Germany) required the development of a specific adhesive (Silorane System Adhesive, 3M ESPE), in particular because of the high hydrophobicity of the silorane composite. The purpose of this study was to characterize the interfacial ultra-structure at enamel and dentin using transmission electron microscopy (TEM).

Methods. Non-demineralized/demineralized 70–90 nm sections were prepared following common TEM specimen processing procedures.

Results. TEM revealed a typical twofold build-up of the adhesive resin, resulting in a total adhesive layer thickness of 10–20 μm. At bur-cut enamel, a tight interface without distinct dissolution of hydroxyapatite was observed. At bur-cut dentin, a relatively thin hybrid layer of maximum a few hundreds of nanometer was formed without clear surface demineralization. No clear resin tags were formed. At fractured dentin, the interaction appeared very superficial (100–200 nm). Distinct resin tags were formed due to the absence of smear plugs. Silver-nitrate infiltration showed a varying pattern of both spot- and cluster-like appearance of nano-leakage. Traces of Ag were typically detected along some part of the enamel–adhesive interface and/or between the two adhesive resin layers. Substantially more Ag-infiltration was observed along the dentin–adhesive interface of bur-cut dentin, as compared to that of fractured dentin.

Conclusions. The nano-interaction of Silorane System Adhesive should be attributed to its relatively high pH of 2.7. The obtained tight interface at both enamel and dentin indicates that the two-step self-etch adhesive effectively bridged the hydrophilic tooth substrate with the hydrophobic silorane composite.

* *Corresponding author.* Tel.: +32 16 33 75 87; fax: +32 16 33 27 52.
E-mail address: bart.vanmeerbeek@med.kuleuven.be (B. Van Meerbeek).
0109-5641/$ – see front matter © 2010 Academy of Dental Materials.Published by Elsevier Ltd. All rights reserved.
doi:10.1016/j.dental.2010.01.010

1. Introduction

Recently, a new class of low-shrinking composites based on silorane technology (Filtek Silorane, 3M ESPE, Seefeld, Germany) was introduced. The silorane resin replaces the conventionally used methacrylate resin matrix within conventional dental composites, thereby providing lower polymerization shrinkage [1–3] as well as better hydrolytic stability [4,5]. Since long, reduced polymerization shrinkage is a highly desired property of composites in order to avoid primary clinically problems that are typically associated with polymerization shrinkage stress, such as there are adhesive-tooth de-bonding, post-operative sensitivity, restoration marginal discoloration and defects, caries recurrence, enamel cracks, etc. [6].

As the resin matrix of the silorane composite significantly differs from that of conventional methacrylate-based composites, a new adhesive needed to be designed and developed to enable bonding of the silorane composite to tooth enamel and dentin. Filtek Silorane therefore comes with a two-step self-etch adhesive, called Silorane System Adhesive (3M ESPE, SSA). It still possesses features of conventional methacrylate adhesives, especially with regard to its bonding mechanism to tooth tissue, while adaptation was needed, especially to make it compatible with the highly hydrophobic silorane matrix. The adhesive somewhat differs from a typical two-step self-etch adhesive, since it involves the application of two resin solutions, of which the first one (Silorane System Adhesive – Self-etch Primer or SSA-Primer) is rather hydrophilic to bond to tooth tissue and the second solution (Silorane System Adhesive – Bond or SSA-Bond) is on the contrary quite hydrophobic in order to adequately bridge the hydrophilic tooth substrate with the hydrophobic silorane composite. For this reason, each resin solution needs to be light-cured separately.

The purpose of this study was to characterize ultramorphologically the interface complex of the low-shrinking silorane composite Filtek Silorane (3M ESPE) bonded to enamel and dentin using the two-step self-etch adhesive Silorane System Adhesive. For this, transmission electron microscopy (TEM) is the method of choice because of its high structural resolution and relatively low artifact incidence.

2. Materials and methods

Six non-carious human third molars were stored in 0.5% chloramine solution at 4 °C and used within one month after extraction. The teeth were randomly divided into 3 groups

Table 1 – Materials used.

Materials	Composition (wt%)	Application
Silorane System Adhesive – Self-Etch Primer Lot. 292319 pH = 2.7 3M ESPE, Seefeld, Germany	15–25% 2-hydroxyethyl methacrylate (HEMA); 15–25% bisphenol a diglycidyl ether dimethacrylate (BIS-GMA); 10–15% water; 10–15% ethanol; 5–15% phosphoric acid–methacryloxy–hexylesters; 8–12% silane treated silica; 5–10% 1,6-hexanediol dimethacrylate; <5% copolymer of acrylic and itaconic acid; <5% (dimethylamino) ethyl methacrylate; <3% DL-camphorquinone; <3% phosphine oxide	(1) Shake the bottle briefly before dosing so that the primer becomes less viscous. (2) Place one drop of primer into the dosing well, then close the dosing well to protect the primer from light and prevent the evaporation of the solvent. (3) Apply the primer to the entire surface of the cavity and massage over the entire area for 15 s. (4) Use a gentle stream of air until the primer is spread to an even film and does not move any longer. (5) Cure the primer for 10 s.
Silorane System Adhesive – Bond Lot. 292274 3M ESPE	70–80% substituted dimethacrylate; 5–10% silane treated silica; 5–10% triethylene glycol dimethacrylate (TEGDMA); <5% phosphoric acid–methacryloxy–hexylesters; <3% DL-camphorquinone; <3% 1,6-hexanediol dimethacrylate	(1) Shake bottle briefly before dosing so that the bond becomes less viscous. (2) Place one drop of bond in the dosing well and close the dosing well to protect the bond from light. (3) Apply the bond to the entire area of the cavity. (4) Use a gentle stream of air until the bond is spread to an even film and does not move any longer. (5) Cure the bond for 10 s.
Filtek™ Silorane Lot. 203905, Shade A3 3M ESPE	5–15% 3,4-epoxycyclohexylethylcyclo-polymethylsiloxane; 5–15% bis-3,4-epoxycyclohexylethyl-phenylmethylsilane; 50–70% silanized quartz;10–20% yttriumfluoride; camphorquinone	(1) The thickness of the individual increments must not exceed 2.5 mm. (2) Cure the filling material for 40 s.

('bur-cut enamel', 'bur-cut dentin' or 'fractured dentin'; see below). All teeth were mounted in gypsum blocks in order to ease manipulation. For the enamel specimens, lingual and buccal enamel was flattened using a medium-grit (100 μm) diamond bur (842, Komet, Lemgo, Germany) in a water-cooled high-speed contra-angle handpiece mounted in the MicroSpecimen Former (The University of Iowa, Iowa, IA, USA). For bur-cut dentin specimens, the occlusal third of the crown was removed at the level of mid-coronal dentin using a slow-speed diamond saw (Isomet 1000, Buehler, lake Bluff, IL, USA), after which a standard smear layer was produced by the medium-grit (100 μm) diamond bur, which was also used to prepare the enamel specimens. From the last two teeth, a shallow 1–2 mm deep groove was cut circumferentially around the tooth at the level of mid-coronal dentin, after which the coronal part was fractured using a forceps to produce a fractured dentin surface free of smear debris. All dentin surfaces were carefully verified for absence of enamel and/or pulp tissue using a stereo-microscope (Wild M5A, Wild Heerbrugg AG, Heerbrugg, Switzerland). The adhesive Silorane System Adhesive (3M ESPE, SSA) with the silorane composite Filtek Silorane (3M ESPE) was then applied, strictly according to the manufacturer's instructions (Table 1). To appraise the ultra-morphological structure of the silorane composite, TEM specimens of two conventional micro-hybrid resin composites (Clearfil AP-X, Kuraray, Okayama, Japan; Filtek Z100, 3M ESPE) were prepared using a silicon mold. Light-curing was performed using an Optilux 500 (Demetron/Kerr, Danbury, CT, USA) device with a light output not less than 600 mW/cm^2. After bonding procedures, specimens were stored for 1 day in tap water at 37 °C.

The specimens were processed for TEM according to the procedure described in detail before by Van Meerbeek et al. [7]. Non-demineralized and lab-demineralized ultra-thin sections were cut (Ultracut UCT, Leica, Vienna, Austria) and examined unstained and positively stained (3% uranyl acetate for 12 min/lead citrate for 13 min) using TEM (JEM-1200EX II, JEOL, Tokyo, Japan). After observation of the resin–enamel interface sections, the TEM grids were additionally exposed for 5 s to 0.1N HCl, and subsequently carefully rinsed with distilled water to remove all dissolved mineral components following a method described before by Hanning et al. [8]. Doing so, the same spots could be imaged by TEM before and after decalcification. In order to reveal potential porous zones in the interface complex, additional specimens were immersed in a 50 wt% ammoniacal silver nitrate solution according to a nanoleakage-detection protocol previously described by Tay et al. [9].

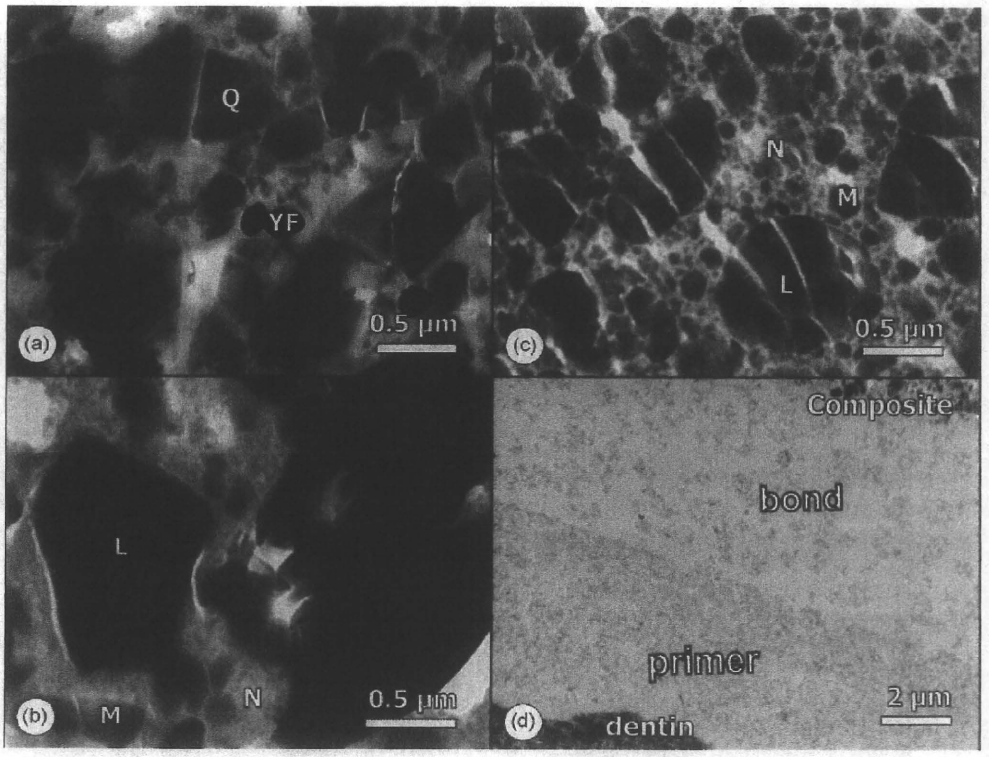

Fig. 1 – TEM photomicrographs of Filtek Silorane and Silorane System Adhesive (bonded to dentin). (a) Filtek Silorane revealed irregularly polyhedral-shaped filler and appeared less loaded than both conventional composites; see (c) and (d). Q, silanized quartz: more electron-lucent, polyhedral-shaped particles with sharp edges (size ranging from 0.05 to 5 μm). YF, yttriumfluoride: irregular, electron-opaque particles with rounded edges. (b) Clearfil AP-X revealed filler particles with rounded edges in three size-ranges. L, large: 1 μm or larger; M, medium: about 0.1 μm; N, nano: nanofiller. (c) Filtek Z100 revealed spherical filler particles. L, large: 1 μm or larger; M, medium: about 0.1 μm; N, nano: nanofiller. (d) SSA revealed an homogenous distribution of the filler within both resin layers. The separately cured SSA-Primer and SSA-Bond did form two distinct layers with different filler content.

3. Results

The ultra-structure of the silorane composite (Filtek Silorane) (Fig. 1a) differed clearly from the two conventional micro-hybrid composites Clearfil AP-X (Fig. 1b) and Filtek Z100 (Fig. 1c). At first, the filler loading of the silorane composite appeared lower than that of both conventional composites. Secondly, the filler particles within the silorane composite are typically irregularly (polyhedral) shaped, while the conventional composites contain filler particles that are more rounded off (Clearfil AP-X) or even spherical (Filtek Z100). Both conventional composites obviously contain three size-ranges of filler particles: large with a diameter of 1 μm or larger, medium with a diameter of about 0.1 μm and small with a nano-sized diameter. The silorane composite lacks nanofiller, but also clear ranges of different sizes could not be observed; actually, any filler size between 0.05 and 5 μm could be observed. Although not different in size, two filler kinds were detected to be present within the silorane composite, namely (1) more electron-lucent, irregularly polyhedral-shaped particles with sharp edges and (2) irregular, electron-opaque particles with rounded edges.

The interaction of SSA with enamel/dentin and with the silorane composite was free of voids in all sections; no de-bonding at any interface occurred during specimen-preparation/imaging. The total thickness of the adhesive resin varied regionally from about 10 to 20 μm. Within the adhesive layer, two distinct layers with different nanofiller concentration could be distinguished, corresponding to the separate application/light-curing of the higher silica-filled SSA-Primer and the lower silica-filled SSA-Bond (Fig. 1d). As initially the amount of filler in SSA-Primer and SSA-Bond is relatively comparable (Table 1: 8–12% and 5–10%, respectively), the observed filler-loading difference is probably due to a concentrating effect in SSA-Primer during solvent removal by air-thinning.

SSA adhesive tightly interacted with bur-cut enamel (Fig. 2). The interaction zone was, however, very thin with mostly only tiny micro-tags observable and without distinct dissolution of hydroxyapatite. Lab-demineralization with HCl disclosed a so-called inter-crystallite nano-retention pattern [8] of less than 1 μm deep, though this widely varied from region to region. SSA adhesive also tightly interacted with bur-cut dentin (Fig. 3). A relatively thin interaction layer of maximum a few hundred nanometers was formed without distinct surface demineralization. The orifices of the dentinal tubules were filled with irregular material, most likely representing smear plugs that were partially impregnated with resin, but without formation of 'true' resin tags. At fractured dentin, the actual interaction of SSA adhesive without smear-layer interference revealed a very thin, 100–200 nm interaction zone without clear signs of surface demineralization (Fig. 4). Distinct resin tags were formed due to the absence of smear plugs. Silver-nitrate infiltration showed a varying pattern of both spot- and

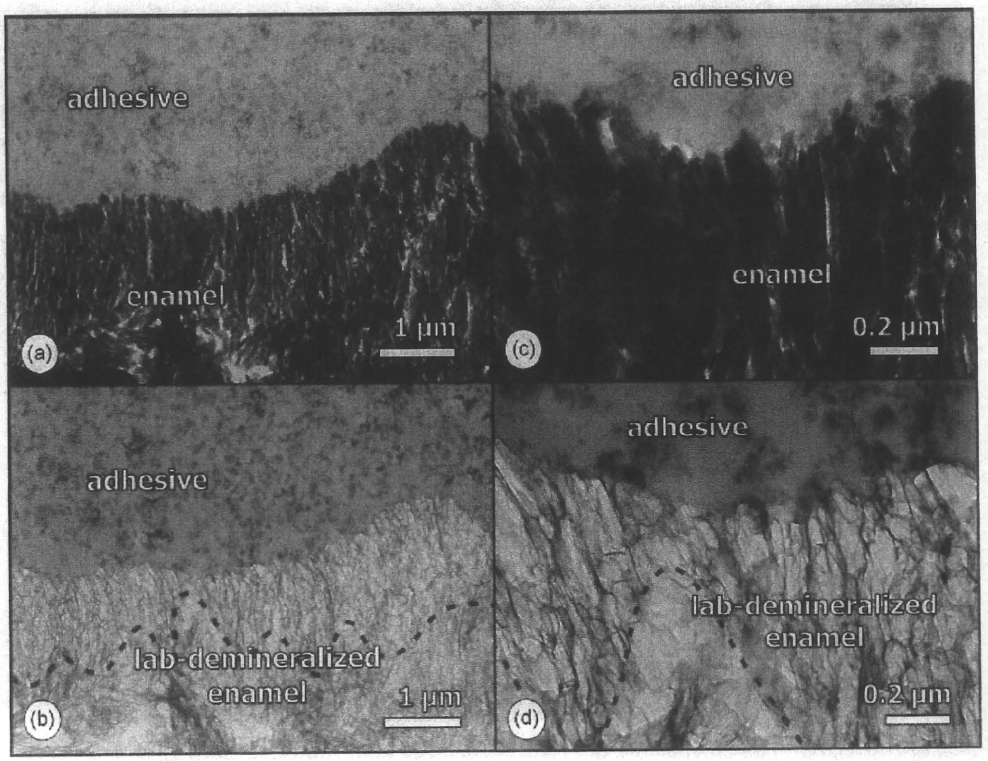

Fig. 2 – TEM photomicrographs of the interface of Silorane System Adhesive bonded to enamel. (a) Overview, showing a tight interface. (b) Corresponding HCl-decalcified section of (a). An inter-crystallite nano-retention pattern of less than 1 μm deep was produced, though this varied widely from region to region. Black dotted line, bottom of intercrystal network. (c) Higher magnification of (a). Visible micro-mechanical interlocking was limited to the present roughness of the enamel surface. (d) Corresponding HCl-decalcified section of (c). The inter-crystallite nano-retention was detected to a depth of less than 1 μm with a huge variety. Black dotted line, bottom of intercrystal network.

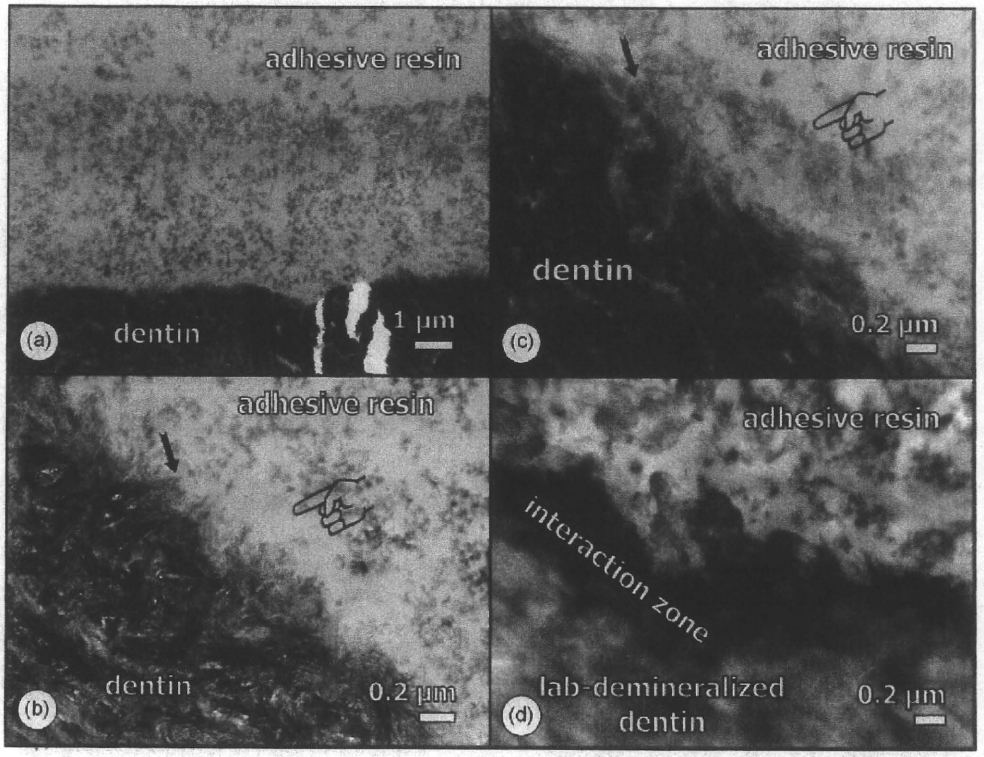

Fig. 3 – TEM photomicrographs of the interface of Silorane System Adhesive bonded to bur-cut dentin. (a) Non-demineralized, unstained section. The actual hybrid layer is difficult to detect, as the interaction with the bur smear layer is somewhat unclear. (b) Non-demineralized, unstained section; higher magnification of the interface between SSA adhesive and dentin. Even at this magnification, it is very difficult to distinguish a distinct hybrid layer (hand pointer). Hydroxyapatite crystals are scattered along the interaction zone (arrow). (c) Non-demineralized, UA/LC stained section. The resin-infiltrated smear layer, containing residual hydroxyapatite, becomes more evident upon heavy-metal staining (hand pointer). Arrow head = hydroxyapatite. (d) Demineralized, UA/LC stained section. The interaction zone reacted heavily with the heavy-metal staining solution. A very shallow zone of collagen exposure, representing the hybrid layer (see also Fig. 4d), can be observed immediately below the resin-impregnated smear.

cluster-like appearance of nano-leakage (Fig. 5), but this varied widely with the region. Substantially more silver-infiltration was observed along the adhesive–dentin interface at bur-cut dentin than at fractured dentin. Noteworthy is also the considerable amount of Ag detected along the SSA-Primer/SSA-Bond interface, along with a spot-like infiltration pattern in SSA-Primer, but not in SSA-Bond (Fig. 5a).

4. Discussion

The key-advantage of Filtek Silorane is low polymerization shrinkage, which is attributed to the new siloxane–oxirane technology [1–3]. Indeed, TEM ultra-structural imaging revealed a filler-matrix organization that significantly differed from that of the two conventional methacrylate-based composites evaluated (Clearfil AP-X, Filtek Z100) with regard to filler loading, distribution and composition (Fig. 1). Both methacrylate-based composites apparently employ a 'smarter' filler distribution, with filler sizes ranging from about 1 µm to nanofiller, increasing the filler volume and decreasing the matrix volume, to the direct benefit of enhanced mechanical properties and reduced polymerization shrinkage. Because of its low-shrinking nature, the silorane composite does not need this 'smart' filler loading to decrease the shrinkage. Also in terms of mechanical properties as flexural strength and hardness, this reduced filler loading seemed no disadvantage [5].

SSA requires separate light-curing of the firstly applied SSA-Primer and the secondly applied SSA-Bond, and consequently differs from typical two-step self-etch adhesives, of which the successive application of a primer and adhesive resin is finalized by only one light-curing step [10] (Table 1). Therefore, SSA's bond to tooth enamel/dentin was established in the first application step, similarly as achieved by one-step self-etch adhesives. One could argue that the name given to this first bottle does not fully meet the definition of a 'conventional' primer. As 'adhesion-promoter', a primer is aimed to promote the infiltration of the subsequently applied, actual 'adhesive resin' or 'bonding resin', while the separately light-cured SSA-Primer can actually be regarded as a one-step self-etch adhesive. Considering its interaction with enamel/dentin is limited to a few hundreds of nanometers, the bonding mechanism involves a form of 'nano-interaction', like it was disclosed before for so-called 'ultra-mild' self-etch adhesives [11,12]. This shallow interaction should be

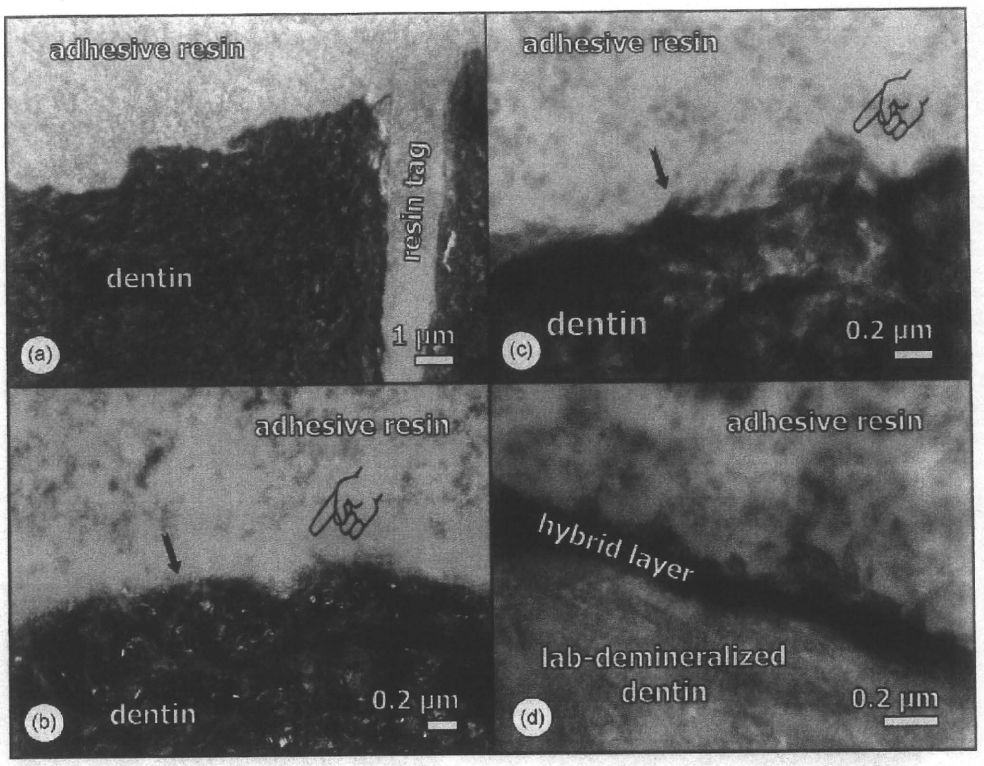

Fig. 4 – TEM photomicrographs of the interface of Silorane System Adhesive bonded to fractured dentin. (a) Non-demineralized, unstained section. The dentin tubules are opened, having enabled the formation of resin tags. (b) Non-demineralized, unstained section; high magnification of the interface between SSA adhesive and dentin. Even at this magnification, it is very difficult to distinguish a distinct hybrid layer (hand pointer). Hydroxyapatite crystals are scattered along the interaction zone (arrow). (c) Non-demineralized, UA/LC stained section. A slight shag-carpet appearance was observed resulting from 'massaging' SSA-Primer (hand pointer). Arrow = hydroxyapatite. (d) Demineralized, UA/LC stained section. A clearly electron dense hybrid layer becomes visible. The very shallow collagen exposure becomes more evident along with the acid-resistant submicron hybrid layer.

attributed to the relatively high pH of SSA-Primer (that also provides better monomer stability and thus longer shelf life) and to its composition consisting of a phosphate-based functional monomer, dimethacrylates (HEMA, Bis-GMA, etc.), a copolymer of acrylic and itaconic acid, silica, and camphorquinone, all dissolved in a water–ethanol solvent (technical data as mentioned in the Material Safety Data Sheet provided by 3M ESPE) (Table 1). The relatively high amount of HEMA keeps this resin solution homogeneous, preventing phase-separation effects like they have been typically documented for HEMA-poor/free one-step adhesives [13].

The secondly applied 'SSA-Bond' is methacrylate-based, but of hydrophobic nature, since it contains a high concentration of substituted dimethacrylate, triethylene glycol dimethacrylate (TEGDMA), silica, a rather low concentration of functional monomer and camphorquinone (according to the Material Safety Data Sheet provided by 3M ESPE) (Table 1). Further details on how this methacrylate-based SSA-Bond links to the silorane composite is currently not known, but according to the technical information provided by 3M ESPE, SSA-Bond contains hydrophobic bifunctional monomers to match the hydrophobic silorane resin. This second hydrophobic adhesive layer is indispensable, as a clear incompatibility exists [14] with the more hydrophilic, one-step experimental precursor of SSA (before being referred to as 'Hermes Bond', 3M ESPE) (Fig. 6). Our TEM adhesive–composite interfacial characterization, on the other hand, did not disclose separations between SSA-Bond and the silorane composite in any of our sections. Besides providing a compatible link to the silorane matrix, the separate application and light-curing of this highly hydrophobic SSA-Bond is also expected to be beneficial with regard to bond stability and long-term bond durability. Actually, it seals off the dentin surface by blocking osmotic water-sorption from dentin [15–18]. Due to the relatively high HEMA-content of the beforehand applied SSA-Primer, the resultant bond would be very vulnerable to water-sorption [19,20], if this second hydrophobic layer would not be applied. Naturally, long-term bond testing needs to confirm how beneficial this solvent-free and separately light-cured resin layer is with regard to bond durability. A point of concern might be the deposition of silver along the interface between the SSA-Primer layer and the SSA-Bond layer (Fig. 5a). Also within the SSA-Primer itself, small silver particles were observed. Both phenomena must most likely be primarily related to the hydrophylicity of the SSA-Primer that contains HEMA and water, the latter being hard to remove from the solution by air-drying. In how far this results in a weak link within the bond complex is currently unknown, nonetheless μTBS-testing revealed failure at

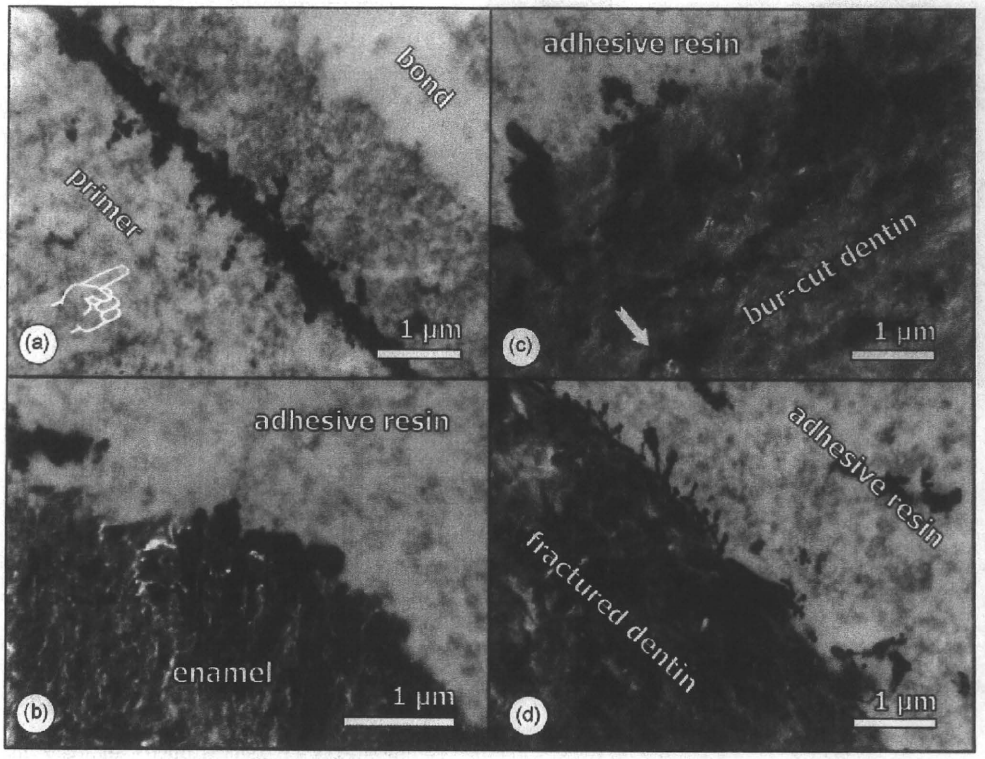

Fig. 5 – TEM photomicrographs of Silorane System Adhesive bonded to enamel/dentin after the specimens were immersed in $AgNO_3$ (nano-leakage screening). (a) The SSA-Primer/SSA-Bond interface. Ag-infiltration was observed in between the two adhesive layers and a spot-like infiltration pattern was seen in SSA-Primer (hand pointer), but not in SSA-Bond. (b) Bur-cut enamel. Ag traces can be detected at some areas along the adhesive–enamel interface. (c) Bur-cut dentin, revealing spot- and cluster-like appearance of nano-leakage. Correct interpretation is difficult, knowing that dentin is such a highly permeable tissue, not only because of its tubules, but also because of the abundant presence of small porosities within intertubular dentin. Arrow = silver appearance in sound dentin. (d) Fractured dentin, revealing relatively small deposits of silver, as compared to that observed at bur-cut dentin, most likely due to absence of surface smear.

this SSA-Primer/SSA-Bond interface rather than at the actual adhesive–dentin interface [21].

When SSA was bonded to bur-cut dentin, a hybrid layer or resin-infiltrated smear layer of maximum a few hundreds of nanometer was formed (Fig. 3). Also, resin tags were not formed, since the smear plugs within the tubules were not dissolved by SSA-Primer. Both the nanometer-size interaction along with absence of tag formation is typical of 'ultra-mild' self-etch adhesives [11,22], when they are applied to the rather thick and compact smear layer produced by a medium-grit diamond bur. Like the ultra-mild self-etch adhesives, SSA-Primer has a pH of 2.7 and revealed a corresponding adhesive–dentin interface morphology [12]. As these ultra-mild self-etch adhesives do only superficially interact with the smear-covered dentin, their bonding effectiveness is largely affected by the properties of the smear layer produced [23]. To assess the actual interaction intensity with dentin, SSA was also applied to fractured dentin that is free from smear (Fig. 4). A much thinner nano-interaction layer was observed than the interaction zone at bur-cut dentin, and represents the 'true' hybrid layer formed without any interference from surface smear. The fractured dentin surface was hardly demineralized, while the adhesive appeared to have penetrated dentin not deeper than 200 nm. At fractured dentin, resin tags were formed, as the tubules were not obstructed by smear, enabling SSA-Primer to have penetrated the dentin tubules effectively.

Despite 'mild' and 'ultra-mild' self-etch adhesives hardly demineralize the surface to provide micro-mechanical interlocking [11,21], they have been shown to provide potential for additional primary chemical interaction with hydroxyapatite that remained available at the enamel/dentin surface. This however depends largely on the actual functional monomer within the adhesive solution [24–26]. With respect to potential chemical interaction of the functional monomer (phosphoric acid–methacryloxy–hexylester) within SSA-Primer, no information is currently available, and would definitely require in-depth chemical analysis using techniques like XPS, XRD or NMR [24,27].

Silver-nitrate impregnation of SSA–dentin interfaces disclosed dense deposits of silver throughout the whole hybrid layer at bur-cut as well as fractured dentin. Substantially more Ag-infiltration was observed along the interfaces of bur-cut dentin, as compared to that of fractured dentin. This consistent pattern of silver deposition resembles the reticular nano-leakage mode observed previously by Tay et al. [9,28]. Besides incomplete resin infiltration, such regions of silver

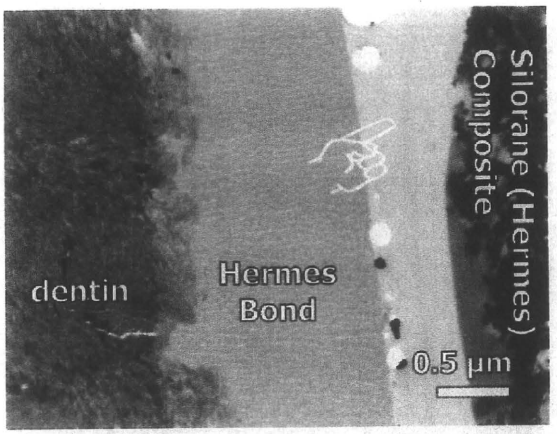

Fig. 6 – TEM photomicrographs of Hermes bond system bonded to bur-cut dentin. Unpublished data; specimens prepared following the same TEM processing (Non-demineralized, unstained section). The interaction of Hermes to dentin is very similar to that of SSA to dentin. At the adhesive–composite interface, on the other hand, a clear separation between the adhesive resin and composite was observed. This happened prior to the TEM processing, as the gap was filled with the epoxy embedding resin (hand pointer).

deposition may also represent sites of retained water, especially typical of HEMA-rich adhesives like SSA-Primer that tend to absorb water more easily [20]. The actual clinical relevance of the nano-leakage pattern detected for SSA remains however unclear [29].

When SSA was bonded to enamel, a tight, but superficial interaction was observed (Fig. 2). Compared to dentin, inter- and intra-crystallite demineralization and subsequent resin infiltration into enamel are more difficult to assess, even by TEM. Hanning et al. [8] developed a TEM specimen-preparation protocol to disclose inter-crystallite nano-retention, as it was produced by the self-etch adhesives. Using this methodology, based on 5-s dipping of a TEM-section into 0.1N HCl, inter-crystallite nano-retention was also disclosed for SSA up to a depth of not more 1 µm and widely varying with the region. This regional variation must probably be related to cracks and fissures that pre-existed within enamel or were produced by bur instrumentation. Immersion of specimens in $AgNO_3$ did reveal some traces of Ag along the adhesive–enamel interface, but this appearance was quite rare and therefore probably not related to bonding deficiencies.

It can be concluded that SSA can be categorized as a two-step self-etch adhesive that bonds to enamel and dentin using a form of nano-interaction, typical of 'ultra-mild' self-etch adhesives and is related to the relatively high pH (2.7) of SSA-Primer. The separately applied and light-cured hydrophobic SSA-Bond is thought to be advantageous with regard to maintaining the interface sealed (longer) against the ingress of water, naturally to the direct benefit of bond durability. Altogether, the tight interface at both enamel and dentin indicates that SSA effectively bridged the hydrophilic tooth substrate with the hydrophobic silorane composite.

Acknowledgements

Dr. Mine has been granted a scholarship of the Government of Flanders to conduct research at the Leuven BIOMAT Research Cluster of the Catholic University of Leuven. This study was supported in part by the Fund for Scientific Research of Flanders (FWO) grant No. G.0206.07, by the KULeuven research grant OT/06/55, by a Joint Research project in the framework of the cooperation between the Japan Society for the Promotion of Science (JSPS) and FWO-Flanders (VS.011.07N), and by 3M ESPE.

REFERENCES

[1] Ernst CP, Meyer GR, Klöcker K, Willershausen B. Determination of polymerization shrinkage stress by means of a photoelastic investigation. Dent Mater 2004;20:313–21.
[2] Weinmann W, Thalacker C, Guggenberger R. Siloranes in dental composites. Dent Mater 2005;21:68–74.
[3] Ilie N, Jelen E, Clementino-Luedemann T, Hickel R. Low-shrinkage composite for dental application. Dent Mater J 2007;26:149–55.
[4] Eick JD, Smith RE, Pinzino CS, Kostoryz EL. Stability of silorane dental monomers in aqueous systems. J Dent 2006;34:405–10.
[5] Ilie N, Hickel R. Macro-, micro- and nano-mechanical investigations on silorane and methacrylate-based composites. Dent Mater 2009;25:810–9.
[6] Ferracane JL. Buonocore Lecture. Placing dental composites—a stressful experience. Oper Dent 2008;33:247–57.
[7] Van Meerbeek B, Yoshida Y, Lambrechts P, Vanherle G, Duke ES, Eick JD, et al. A TEM study of two water-based adhesive systems bonded to dry and wet dentin. J Dent Res 1998;77:50–9.
[8] Hanning M, Bock H, Hoth-Hanning W. Inter-crystallite nanoretention of self-etching adhesives at enamel imaged by transmission electron microscopy. Eur J Oral Sci 2002;110:464–70.
[9] Tay FR, Pashley DH, Yoshiyama M. Two modes of nanoleakage expression in single step adhesives. J Dent Res 2002;81:472–6.
[10] Van Meerbeek B, De Munck J, Yoshida Y, Inoue S, Vargas M, Vijay P, et al. Buonocore memorial lecture. Adhesion to enamel and dentin: current status and future challenges. Oper Dent 2003;28:647–60.
[11] De Munck J, Van Meerbeek B. The current status of bonding to dentin anno 2007. Int J Oral Med Sci 2007;6:45–60.
[12] Koshiro K, Sidhu SK, Inoue S, Ikeda T, Sano H. New concept of resin–dentin interfacial adhesion: the nanointeraction zone. J Biomed Mater Res B: Appl Biomater 2006;77:401–8.
[13] Van Landuyt KL, De Munck J, Snauwaert J, Coutinho E, Poitevin A, Yoshida Y, et al. Monomer-solvent phase separation in one-step self-etch adhesives. J Dent Res 2005;84:183–8.
[14] Ernst CP, Galler P, Willershausen B, Haller B. Marginal integrity of class V restorations: SEM versus dye penetration. Dent Mater 2008;24:319–27.
[15] Tay FR, Pashley DH, Suh BI, Carvalho RM, Itthagarun A. Single-step adhesives are permeable membranes. J Dent 2002;30:371–82.
[16] Tay FR, Lai CN, Chersoni S, Pashley DH, Mak YF, Suppa P, et al. Osmotic blistering in enamel bonded with one-step self-etch adhesives. J Dent Res 2004;83:290–5.

[17] Van Landuyt KL, Snauwaert J, De Munck J, Coutinho E, Poitevin A, Yoshida Y, et al. Origin of interfacial droplets with one-step adhesives. J Dent Res 2007;86:739–44.
[18] Reis A, Albuquerque M, Pegoraro M, Mattei G, Bauer JR, Grande RH, et al. Can the durability of one-step self-etch adhesives be improved by double application or by an extra layer of hydrophobic resin? J Dent 2008;36:309–15.
[19] Tay FR, King NM, Chan KM, Pashley DH. How can nanoleakage occur in self-etching adhesive systems that demineralize and infiltrate simultaneously? J Adhes Dent 2002;4:255–69.
[20] Van Landuyt KL, Snauwaert J, Peumans M, De Munck J, Lambrechts P, Van Meerbeek B. The role of HEMA in one-step self-etch adhesives. Dent Mater 2008;24:1412–9.
[21] Van Ende A, De Munck J, Mine A, Lambrechts P, Van Meerbeek B. Does a low-shrinking composite induce less stress at the adhesive interface? Dent Mater 2010;26: 215–22.
[22] Sarr M, Kane WA, Vreven J, Mine A, Van Landuyt KL, Peumans M, Lambrechts P, Van Meerbeek B, De Munck J. Micro-tensile bond strength and interfacial characterization of eleven contemporary adhesives bonded to bur-cut dentin. Oper Dent 2010;35:94–104.
[23] Ermis RB, De Munck J, Cardoso MV, Coutinho E, Van Landuyt KL, Poitevin A, et al. Bond strength of self-etch adhesives to dentin prepared with three different diamond burs. Dent Mater 2008;24:978–85.
[24] Yoshida Y, Van Meerbeek B, Nakayama Y, Snauwaert J, Hellemans L, Lambrechts P, et al. Evidence of chemical bonding at biomaterial–hard tissue interfaces. J Dent Res 2000;79:709–14.
[25] Yoshida Y, Nagakane K, Fukuda R, Nakayama Y, Okazaki M, Shintani H, et al. Comparative study on adhesive performance of functional monomers. J Dent Res 2004;83:454–8.
[26] Yoshioka M, Yoshida Y, Inoue S, Lambrechts P, Vanherle G, Nomura Y, et al. Adhesion/decalcification mechanisms of acid interactions with human hard tissues. J Biomed Mater Res 2002;59:56–62.
[27] Fukegawa D, Hayakawa S, Yoshida Y, Suzuki K, Osaka A, Van Meerbeek B. Chemical interaction of phosphoric acid ester with hydroxyapatite. J Dent Res 2006;85:941–4.
[28] Tay FR, Pashley DH. Water treeing–a potential mechanism for degradation of dentin adhesives. Am J Dent 2003;16:6–12.
[29] Van Meerbeek B. The "Myth" of nanoleakage. J Adhes Dent 2007;9:491–2.

Relationship between a chronically painful trapezius muscle and its metabolic state analyzed with PET/CT

Satoru Takiguchi, DDS, PhD,[a] Kenji Maekawa, DDS, PhD,[b] Tsuyoshi Ono, DDS, PhD,[a] Nobuya Sasai, MD, PhD,[c] Mitsumasa Kaji, MD, PhD,[d] Glenn T. Clark, DDS, MS,[e] and Takuo Kuboki, DDS, PhD,[f] Okayama, Japan; and Los Angeles, California
OKAYAMA UNIVERSITY, OKAYAMA DIAGNOSTIC IMAGING CENTER, AND UNIVERSITY OF SOUTHERN CALIFORNIA

Objectives. The aim of this study was to investigate the intramuscular metabolic state in chronically painful muscles using positron-emission tomography/computerized tomography (PET/CT).
Study design. The study included 140 consecutive noncancer subjects who underwent PET/CT screening for a physical checkup (mean age 56.0 ± 10.22 y). The demographic data and information on pain in the neck/shoulder region were obtained using a questionnaire. The subjects who had an awareness of pain in the neck/shoulder region for >6 months were regarded to be pain subjects (n = 39). The minimal and maximal standardized uptake values (SUV) of [^{18}F]fluorodeoxyglucose (^{18}F-FDG) of the trapezius muscle in each subject were automatically calculated.
Results. The unpaired *t* test revealed that both the minimal and the maximal SUVs were significantly lower in the pain subjects than in the asymptomatic subjects. A multiple linear regression analysis also demonstrated a significant association between pain in the neck/shoulder region and the SUVs in the trapezius muscle.
Conclusions. Uptake of ^{18}F-FDG was lower in the chronically painful trapezius muscle. **(Oral Surg Oral Med Oral Pathol Oral Radiol Endod 2010;110:54-61)**

The life-time prevalence of chronic orofacial and cervical muscle pain syndrome is currently estimated to be >70% in the general population,[1] and such syndromes are considered to substantially adversely affect patients' quality of life.[2] Although significant effort has been devoted to determining the pathophysiology of chronic muscle pain conditions, the exact mechanisms still need further study. Several years ago, localized disturbances in intramuscular blood flow in chronically painful muscle were reported by several researchers and they assumed that a diminished blood flow caused hypoxia and local metabolic changes (e.g., accumulation of toxic metabolites) as a component of the mechanism of this disorder.[3-5] Regarding the hypoperfusion theory, Delcanho et al.,[4] using near-infrared spectroscopy, demonstrated a significantly decreased level of perfusion in the masseter muscle immediately after maximal isometric contractions in subjects with chronically painful masticatory muscles. Using the same method, Acero et al.[6] compared the intramuscular hemodynamic changes induced by cold pressor stimulation (CPS) between chronic trapezius muscle pain subjects and normal control subjects. They reported that, in the muscle pain subjects, the intramuscular blood flow increase during CPS was significantly diminished compared with the asymptomatic control subjects.

Little is known regarding the local metabolic state in chronic muscle pain patients. Rosendal et al.[5] evaluated the local metabolic conditions in painful muscles of chronic trapezius myalgia subjects. They sampled the interstitial components using microdialysis techniques and compared the interstitial lactate and pyruvate concentrations in trapezius muscles between female chronic trapezius myalgia subjects and healthy female control subjects. The concentrations of those substances were suggested to be significantly higher in the trapezius myalgia subjects than in the controls. They also reported that the concentrations of both

Presented as a preliminary report at the 12th World Congress on Pain, August 20, 2006, Glasgow, Scotland, United Kingdom.
Supported in part by grants-in-aid for scientific research from the Japan Society for the Promotion Science (no. 18659572).
[a]Clinical Researcher, Department of Oral Rehabilitation and Rehabilitation Medicine, Okayama University Graduate School of Medicine, Dentistry, and Pharmaceutical Sciences.
[b]Assistant Professor, Department of Oral Rehabilitation and Rehabilitation Medicine, Okayama University Graduate School of Medicine, Dentistry, and Pharmaceutical Sciences.
[c]Executive Vice President, Okayama Diagnostic Imaging Center.
[d]President, Okayama Diagnostic Imaging Center.
[e]Professor and Chair Division of Diagnostic Sciences, University of Southern California School of Dentistry.
[f]Professor and Chair, Department of Oral Rehabilitation and Rehabilitation Medicine, Okayama University Graduate School of Medicine, Dentistry, and Pharmaceutical Sciences.
Received for publication Aug 14, 2009; returned for revision Feb 15, 2010; accepted for publication Feb 21, 2010.
1079-2104/$ - see front matter

doi:10.1016/j.tripleo.2010.02.028

substances in the trapezius myalgia subjects in response to exercise significantly increased and then returned to baseline levels after stopping exercise. However, the concentrations did not increase in response to exercise in asymptomatic controls. They concluded that trapezius myalgia was associated with an increased anaerobic metabolism. However, one major drawback of this microdialysis technique is that the muscle tissue becomes damaged by the insertion of the catheter, which might alter the metabolic activity. A solution would be to assess the intramuscular metabolic activity using a relatively noninvasive method such as positron- emission tomography (PET). PET is known to detect the glucose metabolism in muscle tissue by measuring the local uptake of [^{18}F]fluorodeoxyglucose (^{18}F-FDG),[7] and it can be performed without local tissue damage. The advantages of this technique are that the metabolic state in muscle tissues can be measured semiquantitatively and the targeted tissue for analysis can be precisely defined from other tissues on the 3-dimensional image created by superimposed computerized tomography (CT).

Using this technique, an investigation of the intramuscular metabolic state was conducted by comparing the ^{18}F-FDG uptake levels in trapezius muscles between chronic neck/shoulder pain and asymptomatic control subjects. A second control condition also was used by comparing the metabolic activity (^{18}F-FDG uptake levels) in the nonpainful gluteus maximus muscles in both groups. The specific aim of the present study was to clarify the characteristics of the glucose metabolism in chronically painful muscles.

MATERIALS AND METHODS

Participants

The participants of this study were selected from 167 consecutive noncancer subjects who underwent PET/CT screening for a physical check-up at the Okayama Diagnostic Imaging Center between May and August 2007 (mean age 56.0 ± 10.19 y; male/female = 114/53). The inclusion criteria of this study were: subjects who agreed to participate before the PET/CT imaging and who completed the questionnaires. The exclusion criteria were: any subject who did not fully fill in the questionnaire on their general health or on their chronic pain conditions regarding their upper body. A total of 27 subjects were excluded due to not filling in the questionnaire, and the final sample consisted of 140 subjects (mean age 56.0 ± 10.22 y; male/female = 95/45). The study protocol was approved by the Ethical Review Board for epidemiology study at Okayama University Graduate School of Medicine, Dentistry, and Pharmaceutical Sciences (approval no. 170).

Questionnaires

The information on each subject was obtained by using 2 different questionnaires. The demographic characteristics of each individual (e.g., gender, age, medical history) were obtained from the standard questionnaire used in the Okayama Diagnostic Imaging Center. In addition, the subjects were asked to answer questions regarding pain in the neck/shoulder region using another questionnaire. The questionnaire addressed the awareness of pain which had continued for >6 months (beyond this period, the pain condition is regarded to be chronic[8]) in the upper body, especially in the neck/shoulder region. If the subject had an awareness of pain in this region, then he/she was further asked to indicate the pain level using a visual analog scale (VAS) of pain. Of 140 subjects, 39 subjects answered yes to the question "Do you have pain in the neck/shoulder region at least once per month, which continues for more than six months?" However, none of these subjects had taken any pain medication because of this or any other pain in their body. Regarding pain severity, no cut-off point was defined, because we wanted to clarify the relationship between the pain level and ^{18}F-FDG uptake levels in trapezius muscle. The subjects were also required to indicate painful body sites on sketches of the human upper body in frontal and rear views. Each subject completed this process before PET/CT scanning.

^{18}F-FDG PET/CT imaging

Each subject refrained from undertaking strenuous forms of exercise the day before and on the day of the PET/CT scanning. They were banned from drinking anything except water and tea at least 5 hours before scanning. The subjects were instructed to sit in a comfortable chair in a quiet room for 90 minutes after intravenous infusion of ^{18}F-FDG (3.7 MBq/kg). After this 90-minute period had passed, whole-body images from the head to thigh (slice thickness 2 mm) were obtained with a PET/CT scanner (Biograph LSO/Sensation 16; Siemens, Erlangen, Germany) in the 3-dimensional mode with the subjects in the supine position.

Analysis of ^{18}F-FDG uptake level

The data of all subjects' PET/CT images were assigned identification numbers, and the following analyses were performed using a blind-to–subject status condition. The PET image and the CT image of each subject were depicted on a personal computer monitor and they were superimposed as a combined PET/CT image. The target muscle whose glucose uptake values were measured in this study was the trapezius muscle, and the gluteus maximus muscle served as a control.

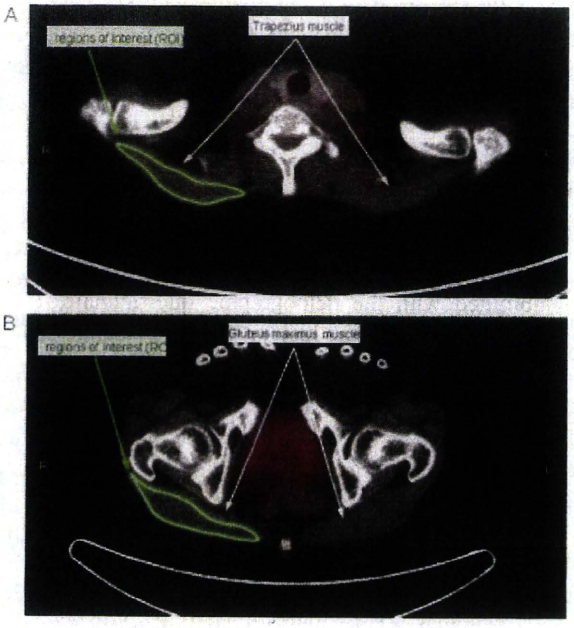

Fig. 1. **A,** Region of interest (ROI) set on the trapezius muscle (study muscle) in positron-emission tomography/computerized tomography (PET/CT) cross-sectional image. **B,** ROI set on the gluteus maximus muscle (control muscle) in a PET/CT cross-sectional image.

The regions of interest (ROIs) were set in the cross-sectional slices of the trapezius muscle and in the gluteus maximus muscle using anatomic landmarks evident on the PET/CT image. The localization of the muscle compartments was verified by comparing the flow images, which provided a topographic distribution of tissue density. The ROIs in trapezius muscle on the images were defined as follows: 1) ROIs were set to contain the upper portion of the trapezius muscle, going by the slice level which depicted the superior end of the acromion; 2) ROIs were manually drawn in the slice to indicate the outline of trapezius muscle; and 3) the same methods for ROI definition were also performed in 2-mm upper and lower slices (Fig. 1, *A*). ROIs of the gluteus maximus muscle were defined as follows: 1) ROIs were set to contain the central portion of the gluteus maximus muscle, going by the slice level that depicted the inferior end of coccyx; 2) ROIs were manually drawn in the slice to indicate the outline of the gluteus maximus muscle; and 3) the same methods for ROI definition were also performed in 2-mm upper and lower slices (Fig. 1, *B*).

As the index of glucose metabolic activity in muscle tissues, the standard uptake values (SUVs) in each ROI were automatically calculated to examine the ^{18}F-FDG uptake quantitatively. SUVs were calculated using the maximum and minimal pixel count within the manually defined ROIs (SUVmax and SUVmin, respectively). The open source image processing software program OsiriX2 (version 3.0.1; Osirix Foundation, Geneva, Switzerland), was used for detecting the SUVs in each ROI. The mean of SUVmax obtained from the ROIs in 3 consecutive slices was regarded as the SUVmax of each subject. The SUVmin in each subject was obtained in the same way. Both the SUVmax and the SUVmin values in trapezius muscle and gluteus maximus muscle were separately calculated. The SUV on the right and left sides of each muscle were separately calculated as well.

Reliability levels of the SUV measurements

Before starting the investigation, the reliability of calculating the SUVs in the trapezius muscle was examined. First, 3 examiners checked and reached a consensus regarding the slice level of the superior end of acromion in the actual PET/CT cross-sectional slice images from 3 randomly selected subjects. Thereafter, the examiners discussed and achieved a consensus regarding the way to depict the outline of the trapezius muscle. After the calibration process, those 3 examiners obtained the SUVmax in both right and left trapezius muscles of 10 randomly selected subjects. After 7 days, the examiners again measured the SUVmax of the trapezius muscles of the same 10 subjects in different image order. The intrarater reliability level was evaluated by calculating intraclass correlation coefficients (ICCs) using the SUVmax obtained by the same examiner before the 7-day interval. The interrater reliability level was also calculated as the ICCs using the SUVmax as measured by 3 examiners.

Statistical analysis

In the respective muscles (trapezius muscle and gluteus maximus muscle), the average of the SUVs in 3 slice levels was computed as the representative SUV of its 1-sided muscle. The average of the SUVs of right- and left-side muscle was computed as the representative SUV of each subject. In the case of subjects who indicated the area only unilaterally in illustrations of upper body, the SUV of the pain present in right- and left-side muscle was defined as the SUV of its subject and then compared with the average of the SUVs of right- and left-side muscle in the subjects without pain.

The relationships between the SUVs and gender, smoking history, diabetes status, the presence/absence of chronic neck/shoulder pain were determined by unpaired *t* test. The correlation between SUVs, age, and the VAS score for pain were determined by Pearson product *r* value. Multiple linear regression analyses were performed using SUVs as outcome variables and the questionnaire items (gender, age, smoking history,

medical history, presence/absence of chronic neck/shoulder pain) as predictor variables. Before performing the multiple linear regression analysis, the selection of predictive variables was needed, because a strong correlation was observed between the presence/absence of neck/shoulder pain and the specific pain levels (VAS pain score). When the predictors, which have a high cross-correlation, are submitted for a multiple linear regression analysis, multicollinearity has been observed.[9] To avoid such statistical inadequacy, the squared multiple correlation coefficients adjusted for the degrees of freedom (R^2) were calculated and compared between the cases in which the presence/absence of pain or the VAS pain score had been submitted for the analysis with other predictors. A P value of $<.01$ was considered to be statistically significant. All statistical analyses were carried out using StatView4.1 software program (Abacus Concepts, Berkeley, CA).

RESULTS

The interrater and intrarater reliability levels of SUV measurement

The interrater and intrarater reliability levels of SUVmax measurement of the ROI, set in the trapezius muscle within a 7-day period, were tested by calculating the ICCs. The mean ICC of interrater reliability was 0.91. The ICC scores of intrarater reliability in each examiner were 0.99 (examiner 1), 0.81 (examiner 2), and 0.96 (examiner 3). Because the ICCs in both interrater and intrarater reliability were considered to be sufficiently reliable,[10] the SUVs measurement in the study was performed by only 1 of the 3 examiners.

SUVs in the trapezius muscle

Figure 2 shows the results of the unpaired t test and the Pearson product r value in analyzing the relationship between SUVs in the trapezius muscle and questionnaire items. The unpaired t test revealed that both the mean SUVmax and the mean SUVmin of the neck/shoulder pain group (n = 39) were significantly lower than that of the pain-free group (n = 101; $P < .0001$). The mean SUVmin of the female subjects was significantly lower than that of the male subjects ($P = .0093$). In addition, the mean SUVmin of the subjects that smoked (n = 37) was significantly higher than that of the nonsmoking subjects (n = 103; $P = .0055$). Statistically significant correlations were observed between the mean SUVmax and the subjects' age ($r = 0.231$; $P = .0058$). In addition, statistically significant correlations were observed between the mean SUVs and the VAS of pain (SUVmax: $r = -0.603$; $P < .0001$; SUVmin: $r = -0.405$; $P < .0001$).

As mentioned in the Materials and Methods section, the squared multiple correlation coefficients adjusted for the degrees of freedom (R^2) were calculated and compared between the cases in which the presence/absence of pain or the VAS of pain score had been submitted for the analysis with other predictors. When the VAS pain score was submitted with the demographic questionnaire items (gender, age, smoking history, medical history) as predictors, the R^2 values were 0.136 (SUVmax in the trapezius muscle) and 0.197 (SUVmin in the trapezius muscle). On the other hand, when the presence/absence of neck/shoulder pain was submitted with the demographic questionnaire items (gender, age, smoking history, medical history) as predictors, the R^2 values were 0.161 (SUVmax in the trapezius muscle) and 0.264 (SUVmin in the trapezius muscle). Because the R^2 values were higher when the presence/absence of neck/shoulder pain was adopted, the following analyses were performed with gender, age, smoking history, medical history, and presence/absence of neck/shoulder pain as predictors.

Table I shows the results of the multiple linear regression analysis when the SUVs in the trapezius muscle were submitted as outcome variables. A significant association was observed between the presence/absence of neck/shoulder pain and the mean SUVmax ($R^2 = 0.161$; $P < .0001$) and the mean SUVmin ($R^2 = 0.264$; $P < .0001$). However, no significant association was observed between the mean SUVs and other predictors.

SUVs in the gluteus maximus muscle

Figure 3 shows the results of the unpaired t tests and the Pearson product r value in analyzing the relation between SUVs in the gluteus maximus muscle and the questionnaire items. Significant correlations were observed between the mean SUVmin and age ($r = 0.386$; $P < .0001$). However, there was no statistical significance between the SUVs in gluteus maximus muscle and the other questionnaire items.

Table II shows the results of the multiple linear regression analysis when the SUVs in the gluteus maximus muscle were submitted as outcome variables. A significant association was seen only between age and the mean SUVmin ($R^2 = 0.169$; $P < 0.0001$).

DISCUSSION

An investigation of the intramuscular metabolic activity in painful muscles may yield better understanding of the pathophysiology of chronic muscle pain conditions. However, previous studies have been carried out by unavoidably using relatively invasive methods (using microdialysis catheters) and it is not hard to imagine how catheter-induced tissue damage itself could induce local metabolic changes. The present study represents the first attempt to clarify the intramuscular metabolic characteristic in chronically painful muscle

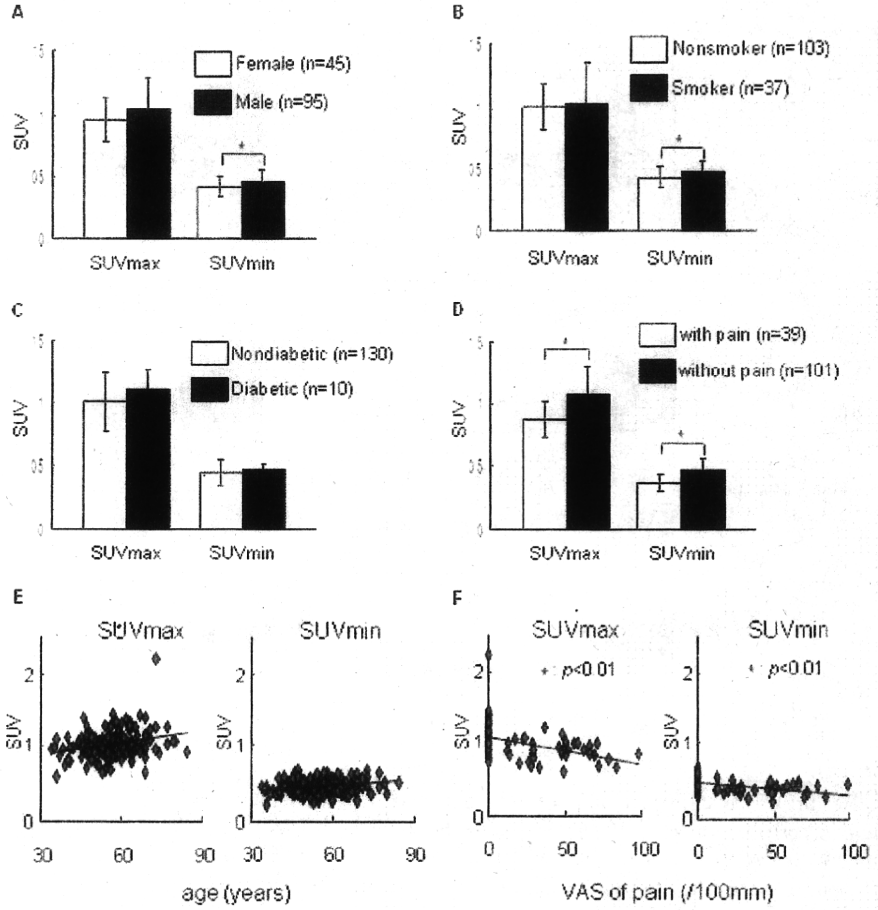

Fig. 2. Results of the statistical analyses, which investigated the relationship between the questionnaire items and standard uptake values (SUVs) in the trapezius muscle. The relationships between the standard uptake values (SUVs) in the trapezius muscle and **(A)** gender, **(B)** smoking history, **(C)** diabetes status, and **(D)** presence/absence of chronic neck/shoulder pain were determined by unpaired *t* test (mean ± SD). The correlation between SUVs in the trapezius muscle and **(E)** age and **(F)** visual analog scale (VAS) score of pain in neck/shoulder region were determined by Pearson product *r* value. $*P < .01$.

Table I. Results of multiple linear regression analysis between SUVs in trapezius muscle and questionnaire items

	SUVmax (F = 6.368) (R = 0.437) (adjusted R^2 = 0.161)		*SUVmin (F = 11.055) (R = 0.539) (adjusted R^2 = 0.264)*	
	Regression coefficient (95% CI)	*P value*	*Regression coefficient (95% CI)*	*P value*
Gender (Male/female)	−0.040 (−0.120-0.040)	.3290	−0.018 (−0.049-0.013)	.2438
Mean age (y)	0.003 (0.001-0.007)	.0601	0.001 (−0.001-0.002)	.2419
Smoker/nonsmoker	−0.013 (−0.096-0.070)	.7521	−0.038 (−0.070-0.006)	.0194
Diabetic/nondiabetic	−0.034 (−0.169-0.101)	.6202	−0.008 (−0.044-0.060)	.7702
Presence of chronic pain in neck/shoulder region (with/without)	0.172 (0.091-0.253)	<.0001*	0.091 (0.060-0.122)	<.0001*

SUV, Standardized uptake value; *CI*, confidence interval.
$*P < .01$.

using a relatively noninvasive method: ^{18}F-FDG PET/CT. In addition to being relatively noninvasive, this method has another advantage in that it can measure the metabolic activity state in muscle tissues semiquantitatively. ^{18}F-FDG is an isotope-labeled glucose-like substance, and when it is intravenously infused the distri-

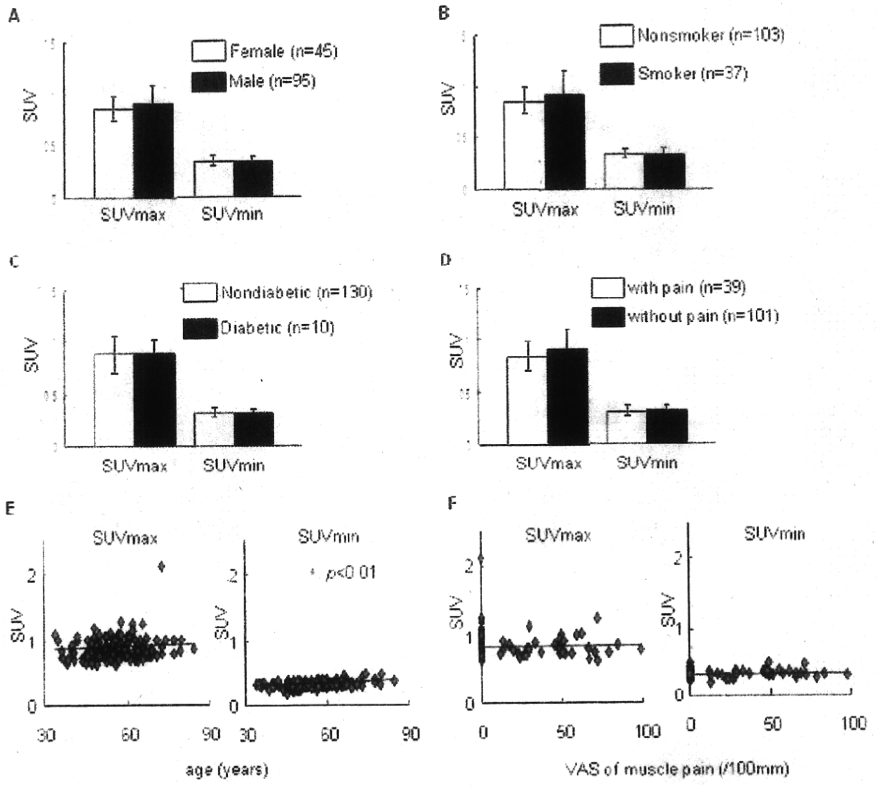

Fig. 3. Results of the statistical analyses, which investigated the relationship between the questionnaire items and SUVs in the gluteus maximus muscle. The relationships between the SUVs in the gluteus maximus muscle and **(A)** gender, **(B)** smoking history, **(C)** medical history, and **(D)** presence/absence of chronic neck/shoulder pain were determined by unpaired *t* test (mean ± SD). The correlation between SUVs in the trapezius muscle and **(E)** age and **(F)** VAS score of pain in neck/shoulder region were determined by Pearson product *r* value. $*P < .01$. Abbreviations as in Fig. 2.

Table II. Results of multiple linear regression analysis between SUVs in the gluteus maximus muscle and questionnaire items

	SUVmax (F = 2.677) (R = 0.300) (adjusted R^2 = 0.056)		*SUVmin (F = 6.712) (R = 0.446) (adjusted R^2 = 0.169)*	
	Regression coefficient (95% CI)	*P value*	*Regression coefficient (95% CI)*	*P value*
Gender (male/female)	−0.043 (−0.108-0.022)	.1940	0.012 (−0.004-0.029)	.1330
Mean age (y)	0.003 (0.001-0.006)	.0266	0.002 (0.001-0.003)	<.0001*
Smoker/nonsmoker	−0.056 (−0.124-0.011)	.0989	−0.020 (−0.037-0.003)	.0230
Diabetic/nondiabetic	0.034 (−0.075-0.143)	.5418	0.015 (−0.013-0.042)	.2883
Presence of chronic pain in neck/shoulder region (with/without)	0.036 (−0.029-0.102)	.2739	0.003 (−0.013-0.020)	.7002

Abbreviations as in Table I.
$*P < .01$.

bution of ^{18}F-FDG in the body is taken as an image by PET scanning. Unlike glucose, ^{18}F-FDG is unresolved for certain fixed periods after intake into muscle cells. Therefore, the ^{18}F-FDG uptake of the muscle tissue is a semiquantitative value that reflects the intensity of glucose metabolism in muscle tissue.

The SUVs in the trapezius muscles of subjects with chronic pain in the neck/shoulder region were found to have a significantly lower uptake of the isotope than was seen in the asymptomatic control subjects. A multiple linear regression analysis revealed that a significant association was observed between the subjective

chronic pain in neck/shoulder region and the SUVs of ^{18}F-FDG in the trapezius muscle. These significant associations were seen for both minimal and maximal SUVs levels. In addition, the Pearson correlation coefficient between both SUVs in the trapezius muscle and the VAS pain score for the neck/shoulder region also indicated a statistically significant negative correlation. This means that the higher the pain level was, the lower the SUVs of ^{18}F-FDG in the trapezius muscle tissues were.

On the other hand, SUVs at a nonpainful muscle site, namely the gluteus maximus muscle, did not differ between the individuals with chronic trapezius muscle pain and asymptomatic subjects. A multiple linear regression analysis did not reveal a significant correlation between SUVs in the gluteus maximus muscle and subject group status. These results suggest the possibility that the local metabolic abnormality arising only in the painful site is associated with a chronic muscle pain pathology.

The main energy sources for muscle tissue are blood glucose and intracellular glycogen. In general, blood glucose intake into muscle cells is enhanced in aerobic conditions. In contrast, blood glucose intake is suppressed in anaerobic conditions and the main energy source is obtained from intracellular glycogen, i.e., the glycolytic pathway is accelerated. Because ^{18}F-FDG is an isotope-labeled glucose-like substance, the lower distribution of ^{18}F-FDG in the painful muscle may indicate that an anaerobic state is facilitated in chronically painful muscle tissue. This assumption coincides with the findings in the Rosendal et al. study,[5] which demonstrated increased anaerobic metabolism by measuring the interstitial pyruvate and lactate concentration in chronic trapezius myalgia subjects. Therefore, the present data provide support for the hypoperfusion theory of chronic regional muscle pain. This theory proposes that a disturbed hemodynamic process leads to a hypoxia state in muscle tissues and this results in anaerobic metabolism in the area.

Another possible mechanism of the phenomenon might be explained by considering the relationship between the muscle activity and its metabolic activity. This means that the lower uptake of ^{18}F-FDG in chronically painful muscle may be caused by decreased muscle activity due to the pain itself. While pros and cons exist, several researchers have reported that there is a muscle hypoactivity state with rest in chronic muscle pain patients.[11] In addition, numerous studies using electromyography revealed that the muscle activity at maximal voluntary contraction is suppressed in chronic muscle pain patients.[12,13] Meanwhile, ^{18}F-FDG PET imaging relies on the principle that active muscle tissue exhibits increased glucose uptake. Therefore, glucose metabolism and ^{18}F-FDG uptake are enhanced in contracting skeletal muscles.[14-16] Sung et al.[17] reported that ^{18}F-FDG PET/CT is useful for detecting the hypermetabolic cervical muscles in patients with idiopathic cervical dystonia. Taken together, the diminished SUVs in chronically painful muscles might be caused by the muscle hypoactivity in chronic muscle pain subjects.

Incidentally, the results of the Pearson correlation coefficient analysis revealed a significantly positive correlation between the SUVmin in the gluteus maximus muscle and the subject's age. The results of the multiple linear regression analysis also indicated the significant association between them ($R^2 = 0.169$; $P < .0001$). These results are consistent with Wehrli et al.'s study,[18] which reported the same trend using other muscles. They investigated the relationship between the SUVs of ^{18}F-FDG in adipose or skeletal muscle tissues and aging using PET/CT. They measured the SUVs of ^{18}F-FDG in the center of the psoas muscle on an axial plane inferior to both kidneys. Although they could not find any statistical significance, the results revealed a decrease in SUV of adipose tissue with aging and the opposite trend in skeletal muscles. Although it is still unclear as to what causes an increase in the muscle metabolic activity with aging, age may be a factor that influences the uptake value of ^{18}F-FDG in the muscle tissue.

Finally, the cross-interaction between intramuscular hemodynamics and this metabolic abnormality has not been directly observed yet. Experimental protocols which thoroughly examine the relationship among various factors such as pain, the metabolic state, the hemodynamics and the muscle activities are necessary to determine the underlying mechanisms of chronic muscle conditions.

CONCLUSION

These findings suggest the possibility that a local metabolic abnormality arising only at the painful site may be associated with chronic muscle pain pathology.

The authors thank the staff members of Okayama Diagnostic Imaging Center for preparing and providing the PET/CT images.

REFERENCES

1. Jensen R. Pathophysiological mechanisms of tension-type headache: a review of epidemiological and experimental studies. Cephalalgia 1999;19:602-21.
2. Macfarlane TV, Blinkhorn AS, Davies RM, Kincey J, Worthington HV. Oro-facial pain in the community: prevalence and associated impact. Community Dent Oral Epidemiol 2002;30:52-60.
3. Lund N, Bengtsson A, Thorborg P. Muscle tissue oxygen pres-

sure in primary fibromyalgia. Scand J Rheumatol 1986;15: 165-73.
4. Delcanho RE, Kim YJ, Clark GT. Haemodynamic changes induced by submaximal isometric contraction in painful and non-painful human masseter using near–infra-red spectroscopy. Arch Oral Biol 1996;41:585-96.
5. Rosendal L, Larsson B, Kristiansen J, Peolsson M, Søgaard K, Kjaer M, et al. Increase in muscle nociceptive substances and anaerobic metabolism in patients with trapezius myalgia: microdialysis in rest and during exercise. Pain 2004;112:324-34.
6. Acero CO Jr, Kuboki T, Maekawa K, Yamashita A, Clark GT. Haemodynamic responses in chronically painful, human trapezius muscle to cold pressor stimulation. Arch Oral Biol 1999;44: 805-12.
7. Williams KV, Bertoldo A, Mattioni B, Price JC, Cobelli C, Kelley DE. Glucose transport and phosphorylation in skeletal muscle in obesity: insight from a muscle-specific positron emission tomography model. J Clin Endocrinol Metab 2003;88: 1271-9.
8. European Federation of IASP Chapters. EFIC's declaration on chronic pain as a major healthcare problem, a disease in its own right. Presented at the European Parliament, Brussels, Belgium, October 9, 2001, after endorsement by 25 European Chapters of the International Society for the Study of Pain. Available at: http://www.efic.org/pain-efic-declaration.php. Accessed April 10, 2010.
9. Yoshioka S. Multicollinearity and avoidance in regression analysis. Behaviormetrika 1986;19:103-20.
10. Krak NC, Boellaard R, Hoekstra OS, Twisk JW, Hoekstra CJ, Lammertsma AA. Effects of ROI definition and reconstruction method on quantitative outcome and applicability in a response monitoring trial. Eur J Nucl Med Mol Imaging 2005;32:294-301.
11. Lund JP, Donga R, Widmer CG, Stohler CS. The pain-adaptation model: a discussion of the relationship between chronic musculoskeletal pain and motor activity. Can J Physiol Pharmacol 1991:69:683-94.
12. Kroon GW, Naeije M. Electromyographic evidence of local muscle fatigue in a subgroup of patients with myogenous craniomandibular disorders. Arch Oral Biol 1992;37:215-8.
13. Andersen LL, Nielsen PK, Søgaard K, Andersen CH, Skotte J, Sjøgaard G. Torque-EMG-velocity relationship in female workers with chronic neck muscle pain. J Biomech 2008;41:2029-35.
14. Tashiro M, Fujimoto T, Itoh M, Kubota K, Fujiwara T, Miyake M, et al. ^{18}F-FDG PET imaging of muscle activity in runners. J Nucl Med 1999;40:70-6.
15. Pappas GP, Olcott EW, Drace JE. Imaging of skeletal muscle function using ^{18}FDG PET: force production, activation, and metabolism. J Appl Physiol 2001;90:329-37.
16. Ohnuma M, Sugita T, Kokubun S, Yamaguchi K, Rikimaru H. Muscle activity during a dash shown by ^{18}F-fluorodeoxyglucose positron emission tomography. J Orthop Sci 2006;11:42-5.
17. Sung DH, Choi JY, Kim DH, Kim ES, Son YI, Cho YS, et al. Localization of dystonic muscles with ^{18}F-FDG PET/CT in idiopathic cervical dystonia. J Nucl Med 2007;48:1790-95.
18. Wehrli NE, Bural G, Houseni M, Alkhawaldeh K, Alavi A, Torigian DA. Determination of age-related changes in structure and function of skin, adipose tissue, and skeletal muscle with computed tomography, magnetic resonance imaging, and positron emission tomography. Semin Nucl Med 2007;37:195-205.

Reprint requests:

Takuo Kuboki, DDS, PhD
Professor and Chair
Department of Oral Rehabilitation and Regenerative Medicine
Okayama University Graduate School of Medicine, Dentistry, and Pharmaceutical Sciences
2-5-1 Shikata-cho, Okayama
Japan 700-8525
kuboki@md.okayama-u.ac.jp